Cavitation simulation on conventional and highly-skewed propellers in the behind-hull condition

Keun Woo Shin[1], Poul Andersen[2], Robert Mikkelsen[2]

[1]MAN Diesel & Turbo, Frederikshavn, Denmark
[2]Department of Mechanical Engineering (MEK), Technical University of Denmark (DTU), Kgs.Lyngby, Denmark

ABSTRACT

The cavitating flows around conventional and highly-skewed propellers in the behind-hull condition are simulated by an in-house RANS solver, EllipSys (Sørensen 2003), with the cavitation model, based on the homogeneous equilibrium modeling (HEM) approach and a vapor transport equation. The validation of the cavitation model in EllipSys has been conducted for the cavitating flows on 2D/3D hydrofoils (Shin 2010).

Prior to the cavitation simulation, the open-water characteristics of the propellers from the computation are compared with those from the propulsion test for the fully-wetted flows (Li & Lundström 2002, Lindell 2005). The cavitation simulation is performed for the flow condition corresponding to that in the cavitation tunnel test for the ship model equipped with the propeller (Johannsen 2004, Lindell 2005). Instead of modeling the hull for the behind-hull condition, the measured wake field in the propeller plane is applied by using a non-homogenously loaded actuator disk (Mikkelsen et al 2007) placed in a plane upstream of the propeller. The variation of the computed cavitation profile with respect to the blade angle is compared with that from the cavitation tunnel test.

The present work describes the study of implementing a HEM cavitation model for computing unsteady cavitation patterns in behind-hull condition with respect to blade angles and cavity extent on the complicated geometry of a conventional/highly-skewed propeller. In the computations, the efficiency of the non-homogeneously loaded actuator disk as behind-hull wake field for the propeller inflow is demonstrated successfully. The computed unsteady cavitation patterns in behind-hull condition and with respect to the blade angle has qualitatively acceptable accuracy, but with respect to the cavity extent, there are quantitative discrepancies.

Keywords

propeller cavitation, RANS, hull wake, actuator disk, highly-skewed propeller

1 INTRODUCTION

The CFD analysis by using a turbulent viscous flow solver is common for practical industrial applications in many disciplines nowadays. Cavitation models for the CFD solvers have been developed in the last decade. The popular type of cavitation models is the HEM with a vapor transport equation. Two-phase mixture is handled as a single-phase fluid with variable fluid properties corresponding to the composition of two phases and phase changes are governed by a transport equation for either vapor volume fraction or vapor mass fraction. Such models have shown the potential for the simulation of propeller cavitation, but the considered cases are limited to the conventional propeller with a moderate skew. In the present work, a cavitation model analogous to the existing models is implemented in EllipSys. The unsteady cavitation on the conventional and highly-skewed propellers in the behind-hull condition is simulated by EllipSys with the implemented cavitation model. The measurement of the behind-hull wake field is applied by the actuator disk, instead of using the inlet boundary condition, so that the well-preserved wake field may reach the region of the propeller flow.

Firstly, the mathematical formulation and numerical schemes for the implementation are summarized. Next, the meshed models are presented and the preliminary validation of the computational models is made for the open-water fully-wetted flow on the propellers. Lastly, the cavitation simulations in the open-water and behind-hull conditions are presented. Before the behind-hull cavitation simulation, the wake field generated by the actuator disk is verified against the intended wake-field measurement only with an axial flow in a rectangular grid.

2 FORMULATION AND IMPLEMENTATION

The constant density and viscosity in the RANS equations for incompressible flows are substituted with variable mixture properties for cavitating flows. The RANS equations are written in Einstein notation and Cartesian coordinates as:

$$\frac{\partial \rho}{\partial t} + \frac{\partial (\rho u_j)}{\partial x_j} = 0 \qquad (1)$$

$$\frac{\partial (\rho u_i)}{\partial t} + \frac{\partial (\rho u_i u_j)}{\partial x_j} = \frac{\partial}{\partial x_j}\left[(\mu + \mu_t)\left(\frac{\partial u_i}{\partial x_j} + \frac{\partial u_j}{\partial x_i}\right)\right] - \frac{\partial p}{\partial x_i} \qquad (2)$$

By adopting the HEM, the mixture properties are approximated on a volume fraction basis as:

$$\rho = \alpha_v \rho_v + (1 - \alpha_v)\rho_l, \mu = \alpha_v \mu_v + (1 - \alpha_v)\mu_l \qquad (3)$$

The vapor volume fraction α_v is obtained by solving the continuity equation for the vapor phase:

$$\frac{\partial (\alpha_v \rho_v)}{\partial t} + \frac{\partial (\alpha_v \rho_v u_j)}{\partial x_j} = -\dot{m} \qquad (4)$$

By the equations (3) and (4), the mass transfer rate $\dot{m}$ between two phases can be related to the material derivative $D\alpha_v/Dt$. By assuming that vapor is distributed as a constant number density of spherical microbubbles with a consistent radius R, $\dot{m}$ is rewritten with R and the time derivative $\dot{R}$ as:

$$\dot{m} = -\frac{\rho_l \rho_v}{\rho}\frac{D\alpha_v}{Dt} = -\frac{\rho_l \rho_v}{\rho}\frac{3\alpha_v \dot{R}}{R} \qquad (5)$$

By integrating the Rayleigh-Plesset equation with ignoring the effects of surface tension, viscosity and non-condensable gas, $\dot{R}$ is expressed as a function of the local pressure p and the initial vapor volume fraction α_{v0} as:

$$\dot{R} = \pm\sqrt{\frac{2}{3}\frac{p_v - p_l}{\rho_l}\left(1 - \frac{\alpha_{v0}}{\alpha_v}\right)} \qquad (6)$$

Eq.(6) is applied to Eq.(5) with the assumption that bubbles grow or collapse rapidly i.e. $R \to R_{max}$, $\alpha_v \to 1$ or $R \to R_{min}$, $\alpha_v \to 4\pi R_{min}^3/3$. By collecting constants into C_e for evaporation and C_c for condensation, $\dot{m}$ is rewritten as:

$$\dot{m} = \begin{cases} -C_e\sqrt{\frac{2}{3}\frac{p_v - p}{\rho_l}}(1 - \alpha_{v0}) & \text{for} \quad p \leq p_v \\[2ex] C_c\sqrt{\frac{2}{3}\frac{p - p_v}{\rho_l}}\alpha_{v0} & \text{for} \quad p > p_v \end{cases} \qquad (7)$$

Most of the cavitation models (Kunz et al 2000, Singhal et al 2002, Zwart et al 2004, Kim & Brewton 2008), based on the HEM, are formulated analogously to Eq.(4) and Eq.(7). It is common that the mass transfer depends firsthand on the local pressure, the amount of liquid for evaporation or vapor for condensation and numerically-determined coefficients.

The integral forms of the partial differential equations (2) and (4) are solved by the collocated finite volume method. By applying Eq.(5) to Eq.(1), the continuity equation is coupled with $\dot{m}$ as:

$$\frac{\partial u_j}{\partial x_j} = \left(\frac{1}{\rho_l} - \frac{1}{\rho_v}\right)\dot{m} \qquad (8)$$

The integral form of Eq.(8) is solved by the SIMPLE method with the Rhie-Chow interpolation.

After the momentum conservation equation (2) is solved for the flow field, the pressure field is corrected by Eq.(8) with $\dot{m}$ from the previous time-step. The eddy viscosity is updated by the k-ω SST turbulence model. The vapor transport equation (4) is solved with the corrected pressure field and α_{v0} from the previous time-step and the mixture properties are updated by Eq.(3).

The expressions in Cartesian coordinates are transformed into those in cylindrical coordinates with a rotating reference frame for the propeller flow. Body force is added to the integral form of the momentum conservation equations to generate a wake field. Based on the Rankine-Froude momentum theory, the local body force $\boldsymbol{F}=(F_r, F_\theta, F_z)$ on the actuator disk corresponds to the intended local wake $\boldsymbol{w}=(w_r, w_\theta, w_z)$ for the uniform inflow velocity V along the axial direction, as:

$$\begin{aligned} F_r &= \rho_l \Delta A (V + w_z)w_r \\ F_\theta &= \rho_l \Delta A (V + w_z)w_\theta \\ F_z &= 0.5\rho_l \Delta A (V^2 - w_z^2) \end{aligned} \qquad (9)$$

Where ΔA = local area element perpendicular to the axial direction. The hydrostatic pressure effects on the cavitation are included by subtracting the relative hydrostatic pressure from the vapor pressure p_v.
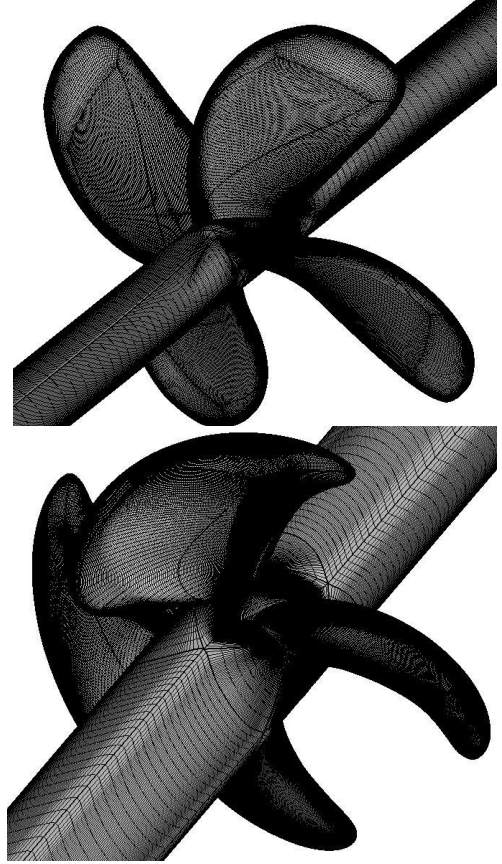

Figure 1 Surface mesh on the conventional (top) and highly-skewed (bottom) propellers

EllipSys uses curvilinear coordinates and parallel computation with the multi-block topology and the MPI.

3 COMPUTATIONAL MODEL

We consider the conventional and highly-skewed propellers, for which the cavitation tunnel tests have been conducted in the open-water and behind-hull conditions on the EU research project Leading Edge. All the reports from Leading Edge are available for the public. The conventional propeller has a model-scale diameter of $D = 0.281$ m and a pitch ratio of $P_{0.7R}/D = 0.701$. The highly-skewed propeller has $D = 0.233$ m and $P_{0.7R}/D = 1.224$.

Figure 1 shows the structured rectangular mesh on the propeller surface. The grid size is decreased around the blade edge to resolve the curvature. The surface mesh is twisted chordwisely to avoid an excessively skewed volume mesh. A cylinder extending through the entire domain with a slip boundary condition substitutes for the propeller hub.

The volume mesh consists of an O-O grid in the near field around the propeller surface and a H-C grid in the far field. The fluid domain extends about $5D$ in all directions from the centre. The cell number is $12.4 \cdot 10^6$ and $18.8 \cdot 10^6$ for the conventional and highly-skewed propellers, respectively. The first-cell height is $1 \cdot 10^{-6} - 3 \cdot 10^{-6}$ m resulting in $y^+ \approx 0.1 - 0.5$.
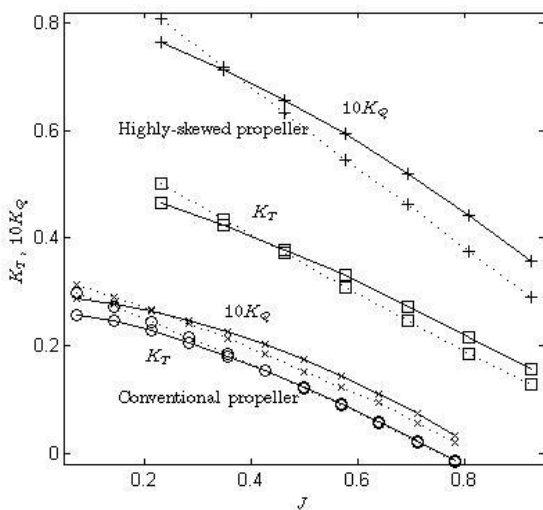

Figure 2 K_T and K_Q from the experiment (dotted line) and computation (solid line) in the open-water condition

Steady-state computations are made for the fully-wetted open-water condition with varying V according to the advance ratio J. The comparison with the experimental result (Li & Lundström 2002, Lindell 2005) in Figure 2 shows underestimation for relatively low values of J and overestimation for higher J in both K_T and K_Q, which may be related to insufficient resolution of high gradients of flow variables for high loadings and increase of turbulent flow error in high local Reynolds number for high J.

4 CAVITATION SIMULATION

4.1 Open-water Cavitating Flow

Steady-state computations are made for open-water cavitating flows with $J = 0.447$, $\sigma_N = 1.60$ on the conventional propeller and $J = 0.603$, $\sigma_N = 2.271$ on the highly-skewed propeller. The cavitation number is defined by

$$\sigma_N = \frac{p_\infty - p_v}{0.5\rho_l N^2 D^2} \tag{10}$$

Where p_∞ = ambient static pressure. The average pressure on the inlet boundary is taken as p_∞ in computation.
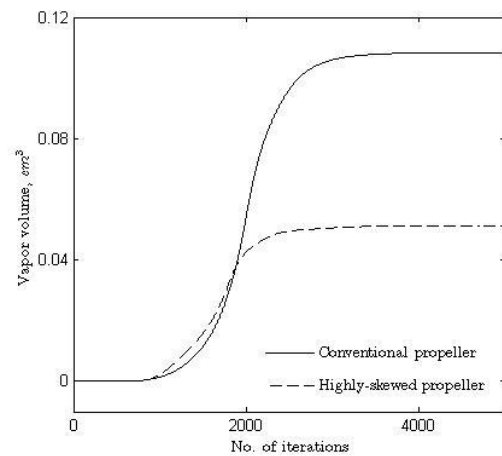

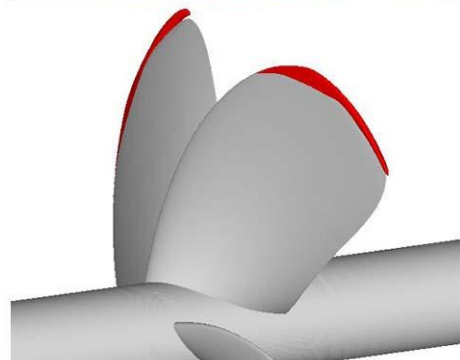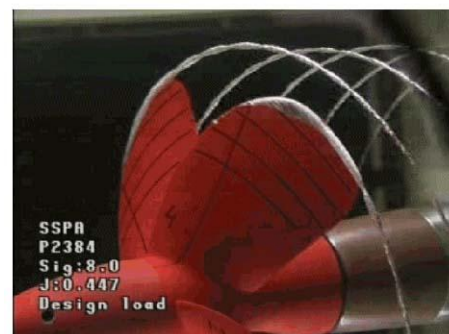**Figure 3 Vapor volume as a function of iteration number**

Figure 4 Snapshot from the experiment (Li & Lundström 2002) (top) and iso-contour of $\alpha_v = 0.1$ from the computation (bottom) for the conventional propeller with $J = 0.447$, $\sigma_N = 1.60$

The ratio between the liquid density and the vapor density is set to $\rho_l/\rho_v = 10000$. The coefficients in the equation for $\dot{m}$ are set to $C_e = 75$, $C_c = 30$. The propeller revolution is set to $N = 14$ rps and 30 rps for the conventional and highly-skewed propellers, respectively. The same revolution of $N = 30$ rps has been applied to the experiment for the highly-skewed propeller, but the applied revolution is not reported in the experiment for the conventional propeller. The solutions are converged with normalized residuals below 10^{-3}. Figure 3 shows that the vapor volume grows with reducing σ_N to an intended value and afterwards it is converged. σ_N is gradually decreased from $\sigma_N = 5$ to an intended value between iteration numbers of 500 and 2000.

In Figure 4 and 5, the iso-contour of $\alpha_v = 0.1$ from the computation is compared to the experimental snapshot. The distribution of the sheet cavity on the suction side has a good agreement with that from the experiment for both propellers. The sheet cavitation continues to be in a form of vortex cavitation, but it is not extended away from the blade surface probably due to a relatively low grid resolution outside the boundary layer.
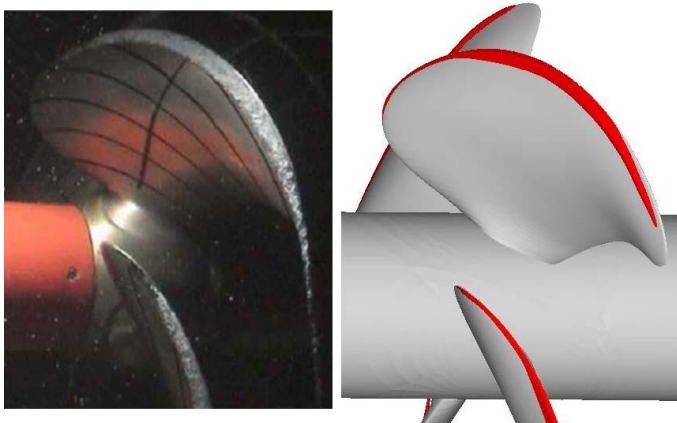

Figure 5 Snapshot from the experiment (Lydorf 2005) (left) and iso-contour of $\alpha_v = 0.1$ from the computation (right) for the highly-skewed propeller with $J = 0.603$, $\sigma_N = 2.271$

4.2 Wake Field Modeling
Before we apply a behind-hull wake field to the cavitation simulation, the wake field, generated by the actuator disk without propeller flow, is verified by the comparison with the intended wake-field measurement (Kuiper 2004). We perform a steady-state computation on the structured rectangular grid with a propeller diameter covering 24 cells in the fine-grid region and an extent of 10D. As shown in Figure 6, the actuator disk is applied to the fine-grid region and the velocity distribution on the cross-section 1D downstream from the actuator disk is taken for the comparison. Only the

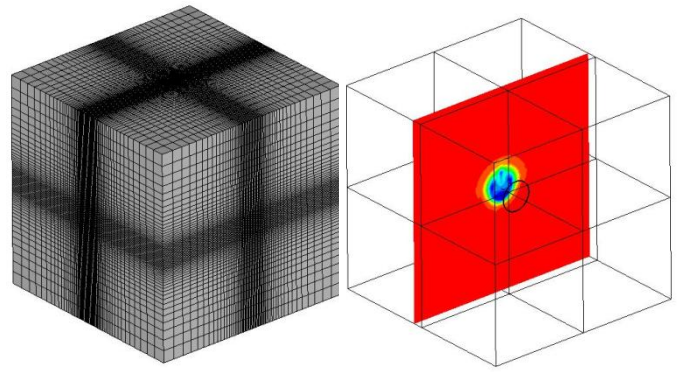axial component of the wake field is applied to the actuator disk.

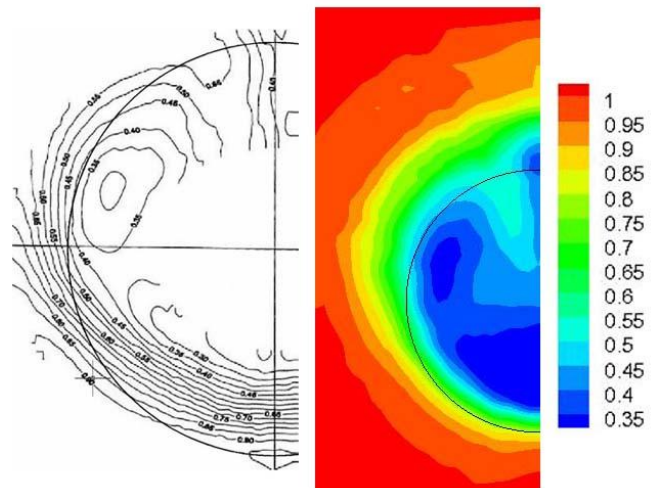**Figure 6 Structured rectangular grid for the wake-field test without propeller flow**

Figure 7 Wake field behind a tanker from the measurement (Kuiper 2004) (left) and the computation (right)
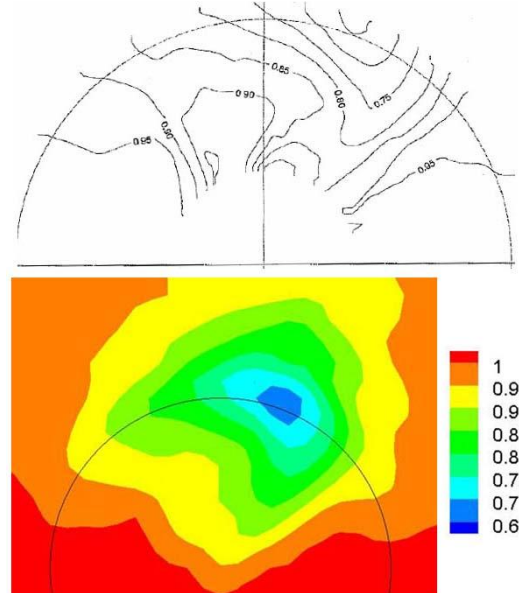

Figure 8 Wake field behind a ferry from the measurement (Kuiper 2004) (top) and the computation (bottom)

The conventional and highly-skewed propellers are designed for a single-screw tanker and a twin-screw ferry, respectively. The wake field from the tanker is

almost symmetric and the wake at inner radii is higher in the lower half, but the wake peak at outer radii exists at the upright angle. The wake field from the ferry is on the port side propeller plane and the left side corresponds to the port side. There is no wake in the lower half and the wake peak appears in the tip region of a blade angle $\varphi = 200°$, where $\varphi = 0°$ indicates the 6 o'clock position. The circle in Figure 7 and 8 indicates the propeller disk area. The propeller disk area for the tanker wake field is roughly approximated, because limited information for the test of the tanker wake-field measurement is available. The normalized axial velocity component $(V-w_z)/V$ is displayed in Figure 7 and 8.

The comparison in Figure 7 and 8 shows that the wake field from the actuator disk agrees well with the measurement in magnitude and distribution.
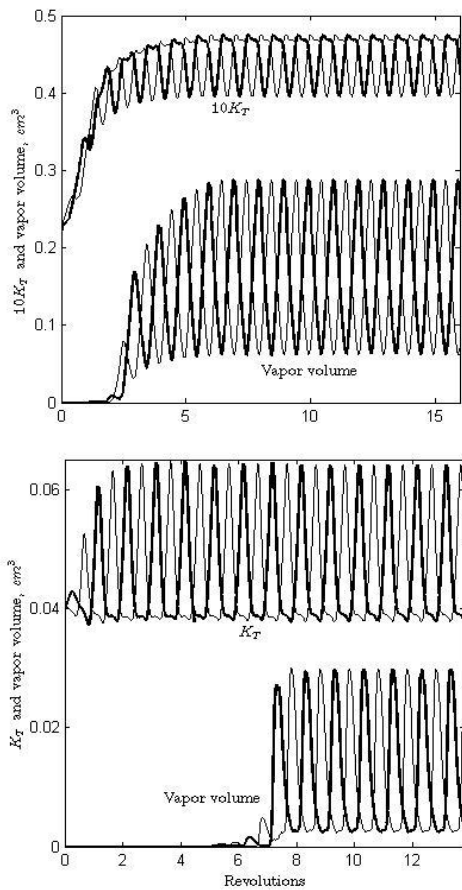

Figure 9 K_T **and vapor volume on each of two opposite blades as functions of time for the conventional (top) and highly-skewed (bottom) propellers in the behind-hull condition**

4.3 Behind-hull Cavitating Flow

We start an unsteady-state computation from the converged solution of the steady-state computation with a time step corresponding to 0.5° rotation of the propeller. First, the actuator disk is applied to a plane 0.5D upstream from the propeller plane. The actuator disk is placed closely to the propeller plane in so far as it is outside the upstream propeller flow in order to

minimize the diffusion of the wake field without a numerical conflict between the propeller flow and the actuator disk. After the wake field is developed, the cavitation number is gradually decreased to the intended value.

We consider a case for $K_T = 0.164$, $\sigma_N = 2.2$ on the conventional propeller. Since the value of J is not reported in the experiment, we find J resulting in a loading similar to K_T from the experiment by applying several different values of J to the computation. In the computation, we use $J = 0.58$ resulting in $K_T = 0.174$.

We consider a case for $J = 0.915$, $\sigma_N = 1.49$ on the highly-skewed propeller. $K_T = 0.176$ is reported in the cavitation tunnel test (Johannsen 2004) and the value of J corresponding to K_T is found from the propulsion test (Mrugowski 2003). In the computation, $J = 0.915$ results in $K_T = 0.183$.

Figure 9 shows that the variations of K_T and vapor volume on each of two opposite blades with respect to time are periodic with the blade rotating frequency. As the wake field is developed, the variation amplitude is increased to a constant. Since the overall magnitude of the wake field from the tanker is higher than that from the ferry, the increase of K_T in the behind-hull condition is also larger. The initial value of K_T is from the open-water computation.
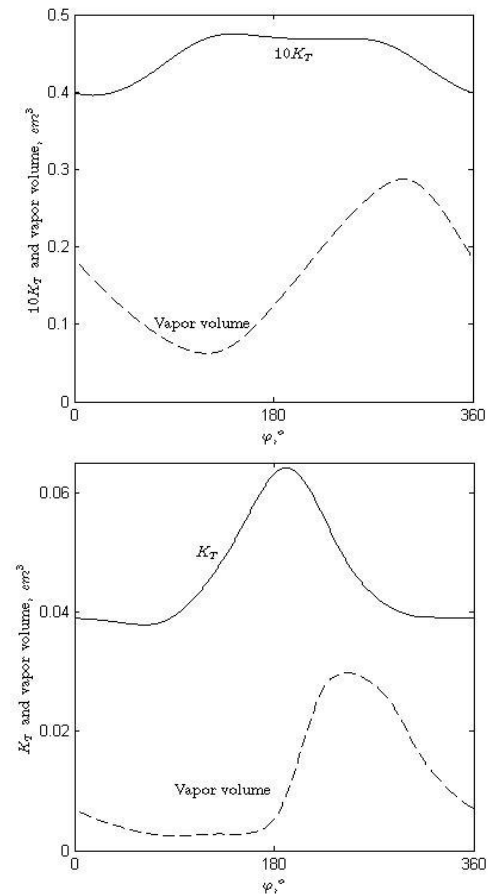

Figure 10 K_T **and vapor volume on a blade as functions of blade angle in a single cycle for the conventional (top) and highly-skewed (bottom) propellers in the behind-hull condition**

Figure 10 shows that K_T is increased, when the blade tip is in a high wake region. While the lower half of the propeller disk area has a high wake in the inner radii for the conventional propeller, K_T is low at $\varphi = 0 - 30°$. It implies that the wake field in the outer radii at the blade tip is more crucial for K_T than that in the inner radii and the effective wake field on the propeller plane is contracted due to the upstream propeller flow. The distribution of K_T with respect to the blade angle for the conventional propeller is not as symmetric along the vertical axis as the applied wake field. The highest peak of K_T is at $\varphi = 190°$ for the highly-skewed propeller. The blade angle is $\varphi = 0°$ for generator line on the 6 o'clock position and the generator line is about 20° ahead of the mid-chord locus for both propellers.

The increase of the vapor volume appears later than that of K_T, which may imply that the formation and collapsing of cavitation bubbles take time. The highest peak of the vapor volume is at $\varphi = 300°$ and 245° for the conventional and highly-skewed propellers, respectively.

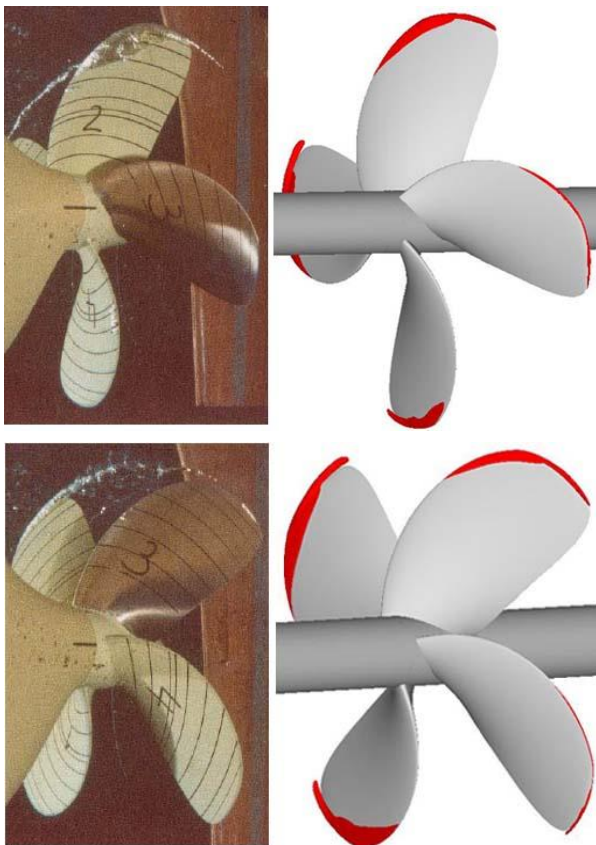whereas the cavitation exists continuously around the whole revolution in the computation. The computed cavitation profile corresponds to the iso-contour of $\alpha_v = 0.1$.

Figure 12 Cavitation profile on the conventional propeller at φ = 0° - 330° with 30° intervals (from top-left corner to bottom-right corner) from the computation for σ_N = 2.2 in the behind-hull condition
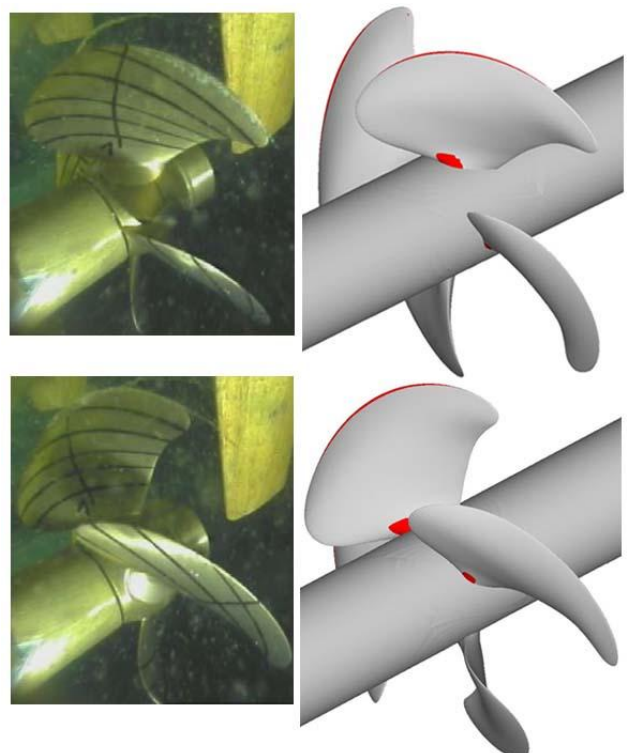

Figure 11 Cavitation on the conventional propeller at φ = 180° (top) and 240° (bottom) from the experiment (Kuiper 2004) (left column) and the computation (right column) for σ_N = 2.2 in the behind-hull condition

Figure 11 shows that the cavitation profile on the conventional propeller changes slowly in the computation rather than in the experiment. The cavitation completely disappears at $\varphi = 280 - 330°$ and appears again at $\varphi = 150 - 180°$ in the experiment,

Figure 13 Cavitation on the highly-skewed propeller at φ = 180° (top) and 210° (bottom) from the experiment (Johannsen 2004) (left column) and the computation (right column) for σ_N = 1.49 in the behind-hull condition

At $\varphi = 180°$, the cavitation profile from the computation is similar to that from the experiment in the starting point at the leading edge of $r \approx 0.75R$ and the transforming pattern from the sheet cavitation to the vortex cavitation, but the chordwise extent at $r \approx 0.75R - 0.9R$ differs. While only the tip vortex cavitation is left at $\varphi = 240°$ in the experiment, the sheet cavitation is still on the increase in the computation.

The cavitation profiles at $\varphi = 180°$ and $240°$ in the experiment are closer to those at $\varphi = 270 - 300°$ and $0 - 30°$, respectively, in the computation. Since the propeller disk area in the applied wake field is roughly chosen, as mentioned above, it is difficult to relate the overall difference to the rates for evaporation and condensation in the cavitation model.

Figure 13 shows that the computed cavitation profile on the highly-skewed propeller at $\varphi = 180°$ and $210°$ start earlier at the leading edge and the extent along the blade tip is less than that from the experiment. No cavitation appears at the outer radii at $\varphi = 90°$ and $120°$ in both the computation and the experiment. Root cavitation appears around the whole revolution in the computation differently from the experiment, because the blade foot is not included in the computational model.

While the experiment shows unstable cavitation in Figure 14, the computation shows no fluctuating cavitation with a higher frequency than the blade rotating rate. Unstable and stable cavitations are marked by single and double diagonal lines in the sketches of the experimental result. Stable cavitation starts to appear at $\varphi = 150° - 180°$ in both the computation and the experiment. The largest extent of the computed cavitation profile appears $10° - 20°$ later than in the experiment. The sheet cavitation disappears at $\varphi = 330° - 340°$. The computed cavitation profiles at $\varphi = 180° - 270°$ are less extended along the chordwise and radial directions than those from the experiment, whereas the variation patterns with respect to the blade angle have similarity.

5 CONCLUSION

The open-water cavitation simulations on the conventional and highly-skewed propellers show an acceptable degree of quantitative accuracy for steady sheet cavitation. The wake field generated by using the non-homogeneously loaded actuator disk shows a high degree of accuracy in a simple rectangular grid without a propeller flow.

The variation pattern with respect to the blade angle of the computed unsteady cavitation in the behind-hull condition has qualitatively acceptable accuracy, but the cavitation extent has quantitative discrepancies, which may be related to the evaporation/condensation rate in the cavitation model and the interaction of the wake field and the propeller flow. If the wake field measured upstream from the propeller plane is applied to the computation, it may reduce the influence of the propeller flow interaction. For a further diagnosis, the cases with simpler wake field and stronger cavitation need to be considered.
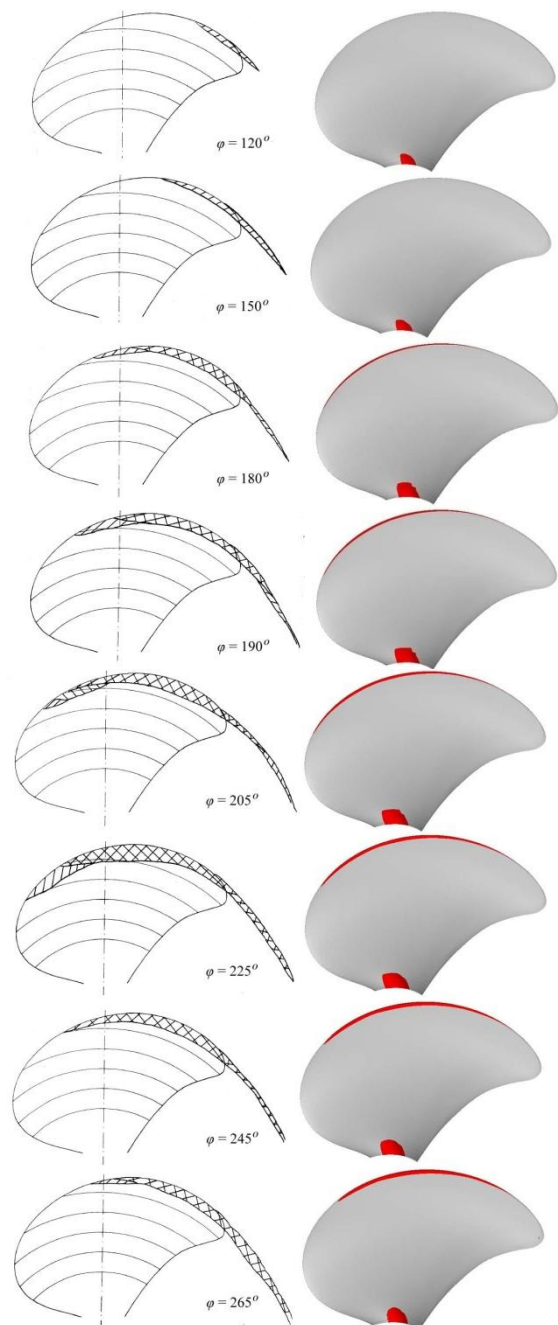

Figure 14 Cavitation profile at the different blade angles on the highly-skewed propeller from the experiment (left column) and the computation (right column)

REFERENCES

Johannsen, C. (2004). Leading edge- Part2: Cavitation tests for a ferry equipped with skew propellers. HSVA Report K51/03, Hamburg, Germany.

Kim, S. E. & Brewton, S. (2008). 'A multiphase approach to turbulent cavitating flows'.

Proceedings of 27th Symposium on Naval Hydrodynamics, Seoul, Korea.

Kuiper, G. (2004). Leading edge: Data of selected propellers. Report No.16206-2-RD, MARIN.

Kunz, R. F., Boger, D. A., Stinebring, D. R., Chyczewski, T. S., Lindau, J. W., Gibeling, H. J., Venkateswaran, S., Govindan, T. R. (2000). 'A preconditioned Navier-Stokes method for two-phase flows with application to cavitation prediction'. Computers & Fluids **29**(8), pp.849-875.

Li, D. Q. & Lundström, P. (2002). Leading edge: open water characteristics and cavitation inception tests of a conventional propeller and a highly skewed propeller. SSPA Report 2870-1, Sweden.

Lindell, P. (2005). Cavitation tunnel tests with final design propeller. SSPA Report 3790-1, Sweden.

Lydorf, U. (2005). Leading edge: Cavitation inception test of a highly skewed propeller. HSVA Report K56-05.

Mikkelsen, R., Andersen, P. & Sørensen, J. N. (2007). 'Modeling of behind condition wake flow in RANS computation on a conventional and high skew propeller'. Proceedings of 10th Numerical Towing Tank Symposium, Hamburg, Germany.

Mrugowski, A. (2003). Leading edge- Part1: Propulsion tests for a ferry equipped with skew propellers. HSVA Report WP 102/03.

Shin, K. W. (2010). Cavitation simulation on marine propellers. PhD Thesis, DTU, Lyngby, Denmark.

Singhal, A. K., Athavale, M. M., Li, H. & Jiang, Y. (2002). 'Mathematical basis and validation of the full cavitation model'. Journal of Fluids Engineering **124**, pp.617-624.

Sørensen, N. N. (2003). General purpose flow solver applied to flow over hills. Risø Report-827(EN), Roskilde, Denmark.

Zwart, P. J., Gerber, A. G. & Belamri, T. (2004). 'A two-phase flow model for predicting cavitation dynamics'. Proceedings of International Conference on Multiphase Flow, Yokohama, Japan.